Draft version June 8, 2023
Typeset using LaTeX default style in AASTeX631

Magnetic Flux Budget in Mean-Field Dynamo Model of Solar Cycles 23 and 24

Valery V. Pipin[1] and Alexander G. Kosovichev[2,3]

[1]*Institute of Solar-Terrestrial Physics, Russian Academy of Sciences, Irkutsk, 664033, Russia*
[2]*Department of Physics, New Jersey Institute of Technology, Newark, NJ 07102*
[3]*NASA Ames Research Center, Moffett Field, Mountain View, CA 94040*

ABSTRACT

We investigate the magnetic flux budget in a previously developed dynamo model of Solar Cycles 23 and 24. The mean-field 3D MHD model simulates the global dynamo process and the magnetic buoyancy instability that leads to the formation of bipolar magnetic regions (BMR) on the solar surface. The initial perturbations of the instability correspond to the distribution of active regions observed during the solar cycles. The toroidal and poloidal flux budgets are calculated by applying the Stokes theorem. The results are compared with a baseline 2D dynamo model without bipolar magnetic regions and with the synoptic observations from Kitt Peak Observatory and SoHO (Solar and Heliospheric Observatory) and SDO (Solar Dynamics Observatory) space missions. We find that while the regions of the high radial rotational shear at the boundaries of the convection zone are important for maintaining the dynamo process, the toroidal magnetic flux that results in the formation of BMR is generated by the latitudinal differential rotation. The toroidal flux generation reaches the maximum at the poles during the solar minima, which explains the correlation between the polar field strength and the subsequent sunspot maximum. However, we find that the generation rate of this flux strongly depends on the radial magnetic field distribution near the solar poles. Our results suggest that while the surface magnetic activity contributes to the poloidal magnetic flux budget, a significant part of the poloidal flux is generated in the deep convection zone, contrary to the Babcock-Leighton solar cycle scenario.

Keywords: Sun: magnetic fields; Sun: oscillations; sunspots

1. INTRODUCTION

The total magnetic flux observed on the solar surface during the 11-year activity cycles is about 10^{24} Mx (Schrijver & Harvey 1984; Schrijver & Harvey 1994). Therefore, at least this amount of magnetic flux must be produced by the large-scale dynamo in the convection zone. But how and where this flux is produced is under debate. A small fraction of it comes from active regions. Depending on the complexity of active regions, the total flux generated by the bipolar sunspot groups (hereafter, bipolar magnetic regions, BMR) is about $4 - -10 \times 10^{22}$ Mx (Nagovitsyn et al. 2016; Abramenko et al. 2023). Some portion of this flux participates in the surface flux transport and in turbulent processes contributing to the global dynamo. Following the basic ideas of Parker (1955), the solar dynamo process cyclically transforms the large-scale poloidal magnetic field into the toroidal field and back by means of the differential rotation and turbulent electromotive force caused by the cyclonic convective motions. Using this scenario, Cameron & Schüssler (2015) (hereafter CS15) showed that the winding up of the surface poloidal magnetic field (given by observations) by the differential rotation is capable of producing the toroidal flux of 10^{24} Mx. This requires the toroidal flux generation rate of about 10^{15} Mx/sec. The winding effect of the differential rotation strongly depends on the toroidal magnetic field strength. This effect can explain the observed relationship between the polar magnetic flux during the solar minimum and the magnitude of the next sunspot activity cycle Schatten et al. (1978); Choudhuri et al. (2007). Following the arguments of CS15, it is tempting to conclude that the poloidal magnetic flux produced by the surface transport of the magnetic flux of bipolar magnetic regions (BMR) is sufficient for maintaining the dynamo operation in the convection zone. Indeed, this idea has been implemented in the Babcock-Leighton flux transport dynamo models (Babcock 1961; Leighton 1969; Choudhuri & Dikpati 1999; Karak et al. 2014; Kumar et al. 2019; Cameron & Schüssler 2017).

However, despite their simplicity and visual appeal in the magnetic 'butterly' diagram, models of this type are not reproduced in the global-Sun 3D MHD simulations. The simulations support the dynamo model suggested by Parker (1955), in which a substantial portion of the toroidal magnetic flux is generated by helical turbulence deep in the convection zone. It is also supported by helioseismic observations of the migrating zonal flows ('torsional oscillations'), which reveal a dynamical pattern corresponding to the dynamo waves predicted by Parker's theory (Kosovichev & Pipin 2019). The self-consistent dynamical mean-field model developed by (Pipin 2018) and (Pipin & Kosovichev 2019, 2020) explained the observed torsional oscillations, including the 'extended' solar cycle phenomenon (Wilson et al. 1988). The model predicted solar-cycle variations of the meridional circulation, which were confirmed by helioseismic observations (Komm et al. 2018; Getling et al. 2021). Further developments include modeling the formation and emergence of bipolar magnetic regions driven by magnetic buoyancy instability (Pipin 2022; Pipin et al. 2022). Thus, this approach combines the essential elements of the Parker and Babcock-Leighton models. The results showed that BMRs could play a substantial role in the dynamo processes and affect the strength of the solar cycles. However, the data-driven modeling, in which the distribution of the initial perturbations that led to the development of BMR followed the distribution of active regions observed during Cycles 23 and 24. Such a data-driven model showed good qualitative agreement with the observations. However, the BMR effect alone could not explain the low amplitude of Cycle 24. It was suggested that this weak cycle and the preceding prolonged minimum could be caused by a decrease of the turbulent helicity in the convection zone during the Cycle 23 declining phase.

In this paper, we investigate the magnetic flux balance in the previously developed mean-field dynamo models of Solar Cycles 23 and 24(Pipin et al. 2022) and compare the modeling results with the corresponding synoptic observations of magnetic fields. The model combines the mean-field turbulent generation effects and generation effects due to the surface BMR activity. This allows us to separate the contributions of the BMR and global dynamo processes in the flux budget. In particular, our aim is to study the role of surface activity in the global dynamo. Section 2 briefly describes the model. In Sections 2 and 3, we present results for the toroidal and poloidal magnetic flux budget and compare them with the synoptic observations. Finally, a summary of the main results is presented in Section 4.

2. DYNAMO MODEL

The model developed by Pipin (2022) (hereafter, P22) and Pipin et al. (2022) (hereafter PKT) includes the full set of mean-field MHD equations: the 3D magnetic induction equation and the energy and anelastic momentum equations in the 2D anelastic approximation. The large-scale magnetic field is decomposed into the sum of the axisymmetric and the nonaxisymmetric components. Its evolution is governed by the induction equation formulated in the mean-field MHD (magnetohydrodynamics) framework of (Krause & Rädler 1980). It describes the magnetic field generation by turbulent helical convection (the α-effect) and includes effects of small-scale magnetic helicity, turbulent pumping, and eddy magnetic diffusivity. The magnetic helicity evolution is governed by the balance of the total magnetic helicity density Mitra et al. (2010). The induction equation includes injection of the bipolar magnetic regions.

The model takes into account the back-reaction of dynamo effects on the global axisymmetric flow evolution. The meridional circulation velocity and the differential rotation are not-prescribed but obtained by solving the momentum equation, which is formulated in terms of the angular momentum balance and the azimuthal vorticity. The model includes the heat transport in the solar convection zone, as well as the effect of rotation on the turbulent stress-tensor. The reference profiles of mean thermodynamic parameters, such as entropy, density, temperature, convective turnover time, and mixing length, are determined from the stellar interior model MESA (Paxton et al. 2013). The convective RMS velocity is determined from the mixing-length approximation. Noteworthy that the large-scale flow and magnetic field evolution results in modulation of the convective heat transport, the mean entropy variations and variations of the turbulent mixing parameters, as well. This effect modulates the global zonal and meridional flows, resulting in the extended solar-cycle variations of these flows. Further details can be found in our previous papers, e.g., Pipin (2022) and Pipin et al. (2022).

The emergence of the bipolar magnetic regions (BMRs) is modeled using the mean electromotive force, which is represented by the α and magnetic buoyancy effects acting on the unstable part of the axisymmetric magnetic field Pipin (2022). The magnetic buoyancy velocity is modeled using the turbulent and mean-field buoyancy effects, suggested by Kitchatinov & Rüdiger (1992); Kitchatinov & Pipin (1993); Ruediger & Brandenburg (1995), taking into account the magnetic tension.

In the data-driven model, the latitudinal and longitudinal coordinates and the perturbation size in the BMR initiation function are taken according to the properties of active regions from the NOAA database of solar active regions

Table 1. The parameters of the model runs. T0 is the axisymmetric baseline model without BMR. S2 in the data-driven model with the BMR emergence. The third column shows the magnitude of the toroidal flux in the convection zone and its generation rate; the fourth column shows the same for the surface flux of the axisymmetric poloidal magnetic field; the column C_α shows the scaling parameter of the global mean-field alpha-effect; the next column shows the time intervals for the corresponding C_α values; the last column shows the duration of the activity cycles (half dynamo periods of the magnetic cycles).

Model	BMR injection	Total toroidal flux and generation rate // [Mx], [Mx/yr]	Total poloidal flux and generation rate // [Mx], [Mx/yr]	C_α	C_α time intervals, [yr]	Cycle Period, [yr]
T0	no injection	8×10^{23}, 3×10^{23}	1.9×10^{22}, 4×10^{21}	0.045	-	10.4
S2	data-driven injection	10^{24}, 4×10^{23}	1.9×10^{22}, 6×10^{21}	0.04 0.035 0.04	$\geq$0 $\geq$5 $\geq$11	11.2, 11.6

(https://www.swpc.noaa.gov/), as described in P22. The radial positions of the unstable points are determined through the whole convection zone using Parker's instability condition (Parker 1984) (see, Pipin et al. 2022). The fluctuation of the BMR helicity parameter (which defines the tilt) is random; that is the tilt was not taken from observational data. The data-driven model starts from the epoch of the solar minimum at the beginning of 1996. Cycles 23 and 24 have different magnitudes and lengths. Using the numerical experiments, we found that the prolonged decay of Cycle 23 can be modeled if we decrease the turbulent helicity, C_α, parameter by 20% relative to its value after five years from the beginning of simulations (in 2001), and we increased it back by 15% in 2007. The initial value is close to the dynamo instability threshold.

To evaluate the effects of BMRs on the dynamo processes and magnetic flux budget, we compare the data-driven model with the axisymmetric reference model T0, calculated without the BMRs, and for a global helicity parameter constant in time. This baseline model shows an agreement of the angular velocity profile with helioseismology results for the angular velocity and meridional circulation. The double-cell meridional circulation is reproduced when the variations of the Coriolis number with depth are taken into account. The secondary circulation does not significantly affect the model results. Therefore, in this paper, we performed calculations for the models with single circulation cells in each hemisphere.

The model parameters are given in the Table 1. We use the same notations for our runs as described in P22.

3. RESULTS

3.1. *Toroidal field budget*

The dynamo models of Pipin (2022) showed the importance of the BMR activity for the whole dynamo process. To estimate variations of the toroidal magnetic flux in the dynamo region, we follow the approach of Cameron & Schüssler (2015) (hereafter CS15) and apply the Stokes theorem to the induction equation. The time derivative of the axisymmetric toroidal magnetic field flux in the Northern hemisphere of the Sun is calculated as follows,

$$\frac{\partial \Phi^{\rm N}_{\rm tor}}{\partial t} = \oint_{\delta\Sigma} \left(\overline{\mathbf{U}} \times \overline{\mathbf{B}} + \boldsymbol{\mathcal{E}} \right) \cdot \mathrm{d}\mathbf{l}, \tag{1}$$

where $\Phi^{\rm N}_{\rm tor} = \int_\Sigma \overline{B}_\phi \mathrm{dS}$, Σ is the area of the meridional cut through the solar convection zone in the hemisphere, $\delta\Sigma$ stands for the contour line confining the cut, and dl is the line element of $\delta\Sigma$. The same can be written for the Southern hemisphere flux $\Phi^{\rm S}_{\rm tor}$.

Similarly to CS15, we estimate the RHS of Eq. (1) in the coordinate system co-rotating with the solar equator: $\overline{U}_{0\phi} = R\sin\theta\Omega_0$, where Ω_0 is the surface angular velocity at the equator.

$$\frac{\partial \Phi^{\rm N}_{\rm tor}}{\partial t} = \int_0^{\pi/2} \overbrace{\left(\overline{U}_\phi - \overline{U}_{0\phi}\right)\overline{B}_r \mathrm{r_t}}^{\rm I_1} \mathrm{d}\theta \tag{2}$$
$$+ \int_{\rm r_i}^{\rm r_t} \overbrace{\left(\overline{U}_\phi^{(\frac{\pi}{2})} - \overline{U}_{0\phi}\right)\overline{B}_\theta^{(\frac{\pi}{2})}}^{\rm I_2} \mathrm{dr}$$
$$+ \int_{\rm r_i}^{\rm r_t} \overbrace{\left(\mathcal{E}_r^{(0)} - \mathcal{E}_r^{(\frac{\pi}{2})}\right)}^{\rm I_3} \mathrm{dr} + \int_0^{\pi/2} \overbrace{\left(\mathcal{E}_\theta^{(\rm t)}\mathrm{r_t} - \mathcal{E}_\theta^{(\rm i)}\mathrm{r_i}\right)}^{\rm I_4} \mathrm{d}\theta$$

here, $r_t = 0.99$R, $r_i = 0.67$R, are the radial boundaries of the dynamo region. The integral kernels, I_1 and I_2, represent magnetic induction $\overline{\mathbf{U}} \times \overline{\mathbf{B}}$ calculated along the surface and along the equatorial radius, respectively. The kernels, I_3 and I_4 represent turbulent electromotive force $\boldsymbol{\mathcal{E}}$ calculated along the radial and azimuthal parts of the integration contour. These contributions in the flux budget equation were considered in CS15. To estimate contributions I_1 and I_2, we use the angular velocity profile from our model.

Figure 1(a-c) shows the time-latitude diagrams of the integral kernel, I_1, calculated for our dynamo models and for the observation data set. In Figure 1(d), we compare the total unsigned flux of the radial magnetic field of the models and observations. The dynamo models show qualitative agreement with the observational results. This agreement results from the qualitative similarity of the axisymmetric magnetic field evolution in the dynamo model and observations. Yet we see some differences. The simulated magnetic flux on the surface is about 5×10^{23} Mx for Cycle 23 and $3.5\cdot10^{23}$ Mx for Cycle 24. The generated flux is solely due to the BMR emergence. It is about factor 3 to 10 higher than the BMR flux estimated from observations by Nagovitsyn et al. (2016); Abramenko et al. (2023), who found the flux in the range of $4 - 10 \times 10^{22}$ Mx. The most significant difference between the models and observations is during the growing phase of the magnetic cycles.

Figure 2 shows the latitudinal profiles of I_{1-3} and the radial profiles of I_{2-4} for model T0 for the period of the magnetic cycle minimum. The results for $I_{1,4}$ are qualitatively similar to the results CS15 derived from observational data. This is expected because our models are in the qualitative agreement with solar observations in terms of the time-latitude evolution of the surface radial magnetic field ('the magnetic butterfly diagram'). The diffusive decay of the toroidal magnetic flux is captured as well because the phase shift between the evolution of the poloidal and toroidal magnetic fields in the dynamo models corresponds to the observations.

The models show a sharp poleward increase of I_1 (Fig. 2a). This effect produces the winding of the poloidal component of the magnetic field by the latitudinal shear and generation of the toroidal field component. The effect of the radial shear, I_2, has a maximum near the bottom of the convection zone, where it is the same order of magnitude as I_1. In the main part of the convection zone, it is less by order of magnitude than near the bottom. In our previous paper, we found that the polar magnetic field in solar observations does not increase toward the poles as much as our models show. This affects the estimations of the budget equation terms. Figure 2a shows that the poleward increase of I_1 is substantially weaker in the case of the constant profiles of the radial magnetic field in the polar regions above 60° latitude. Figure3 illustrates the latitudinal profiles of I_1 for the minima of Cycles 22, 23, and 24 in our dynamo models and the observations. In all cases, we see that the observations show a step-like increase of I_1 above 50° latitude and almost uniform I_1 is near the solar poles. The dynamo models show qualitatively similar profiles, but the distribution of I_1 is not uniform near the poles.

Figure 4a shows the time evolution of the RHS contributions of Eq. 2. Noteworthy, these variations in the Southern hemisphere have the opposite sign (see CS15). We see that the integral of I_2 is about a factor of two smaller than the integral of I_1. This is because the radial shear changes sign along the radius. Figure 4b shows phase diagrams illustrating the budget of the toroidal flux generation rate (horizontal axis) and the loss rate (vertical axis) in our dynamo models. The flux budget parameters are larger than those deduced by CS15 from solar observations. The difference is because of the additional generation and loss terms included in our models. Also, the behavior of the radial magnetic field near the poles affects the budget considerably. If we apply the constant profiles of the radial magnetic field in the polar regions above 60° latitude for Model T0, we find our results become close to those by CS15.

Figure 5 shows the axisymmetric toroidal magnetic field (images in top panels) and contour lines of the vector potential of the poloidal field, and the corresponding toroidal flux generation rate (bottom panels) in the convection zone in Model S2 during Cycle 23. The vector-potential contour lines correspond to the poloidal field lines. These images and the accompanying animation illustrate the dynamo wave and help to understand the effects of the radial and latitudinal gradients of the angular velocity on the large-scale poloidal magnetic field. Stretching of the poloidal field lines due to the rotational gradients leads to the toroidal field generation. We see that in the lower part of the convection zone, the radial gradient of the angular velocity stretches the closed part of the axisymmetric poloidal magnetic field. It results in the opposite signs of the toroidal flux generation rate in the lower and upper part of the convection zone. Simultaneously, it produces the dynamo wave propagation along the radius following the Parker-Yoshimura rule (Yoshimura 1975). The latitudinal shear stretches the open part of the poloidal flux in the upper part of the dynamo domain. The positive sign of the α-effect in the Northern hemisphere results in a coordinated action of the radial and latitudinal shear in the upper part of the convection zone. It follows that the radial gradient provides a substantial part of the toroidal flux inside the convection zone and affects the mean magnitude of the toroidal flux there. The role of the open poloidal flux and the latitudinal shear is to control the seeding magnitude of the subsequent cycle. This affects the correlation of the polar magnetic field parameters with the magnitude of the toroidal field dynamo wave of the subsequent magnetic cycle.

3.2. *The poloidal field flux budget*

The axisymmetric poloidal magnetic field can be defined through the azimuthal component of the vector-potential, i.e.,

$$\overline{\mathbf{B}}_P = \boldsymbol{\nabla} \times \left(\hat{\boldsymbol{\phi}} A\right).$$

Therefore, by applying the Stokes theorem for the poloidal flux in the Northern hemisphere, we have

$$\int_N \overline{\mathbf{B}}_P \cdot \mathrm{d}\mathbf{S} = \int_N \boldsymbol{\nabla} \times \left(\hat{\boldsymbol{\phi}} A\right) \cdot \mathrm{d}\mathbf{S} = \oint_{\boldsymbol{\ell}} A \hat{\boldsymbol{\phi}} \cdot \mathrm{d}\boldsymbol{\ell}, \tag{3}$$

where $\boldsymbol{\ell}$ is the boundary oriented along the equator line. The total surface flux of the poloidal magnetic field though the Northern hemisphere at radius r is $\Phi_N = 2\pi r A(\pi/2, r)$; and for the South hemisphere $\Phi_S = -\Phi_N$. The rate change of Φ_N is determined by the vector potential evolution,

$$\partial_t A = \mathcal{E}_\phi + \left(\overline{\mathbf{U}} \times \overline{\mathbf{B}}\right)_\phi. \tag{4}$$

The second term of this equation represents the effect of the meridional circulation. Both the solar observations (Komm et al. 2015; Getling et al. 2021; Komm 2022) and our dynamo models predict $\overline{U}_\theta \approx 0$ at the equator. It is exactly $\overline{U}_\theta = 0$ for the nonmagnetic case. Another effect of the meridional circulations is due to the trans-equatorial magnetic field and $\overline{U}_r$. The latter one is exactly zero at the surface. The mean electromotive force has three different contributions: generation, $\mathcal{E}_\phi^\alpha$, turbulent pumping, $\mathcal{E}_\phi^\gamma$, and turbulent diffusion $\mathcal{E}_\phi^\eta$,

$$\mathcal{E}_\phi = \mathcal{E}_\phi^\alpha + \mathcal{E}_\phi^\gamma + \mathcal{E}_\phi^\eta. \tag{5}$$

Figure 6 shows the surface evolution of the different terms of Eq. (4) for Model S2. We find that the surface evolution of the vector potential is dominated by the radial part of the turbulent diffusion and the surface meridional circulation, i.e., Fig. 6(b), can be reproduced in great detail by the sum of the terms shown in Figure 6(c–d). Interesting that the equatorial vector potential, which can be used as a proxy for the generation of the poloidal flux, is solely dependent on the diffusive part, $\mathcal{E}_\phi^\eta$ (see Figure 6 b,c and e). The magnitudes of $\mathcal{E}_\phi^\alpha$ and the latitudinal diffusive transport are of the same order of magnitude, but they are considerably smaller than the other terms of Eq. (4).

The generation of the poloidal flux from the toroidal flux by means of the α-effect and the emerging bipolar magnetic regions become essential already in a shallow layer below the surface (Pipin 2022). Following that paper, we decompose $\mathcal{E}_\phi^\alpha$ as follows,

$$\mathcal{E}_\phi^\alpha = \left(\overline{\alpha}_{\phi\phi}^{(H)} + \overline{\alpha}_{\phi\phi}^{(M)}\right) B + \overline{\tilde{\alpha}_{\phi\phi}\tilde{B}_\phi} + \overline{\alpha_\beta \langle B \rangle_\phi}, \tag{6}$$

where $\overline{\alpha}_{\phi\phi}^{(H)}$ is the hydrodynamic part of the α effect, $\overline{\alpha}_{\phi\phi}^{(M)}$ is α-effect due to the small-scale magnetic helicity, $\overline{\tilde{\alpha}_{\phi\phi}\tilde{B}_\phi}$ is the azimuthal average of the nonlinear α effect of the nonaxisymmetric magnetic field, $\tilde{B}_\phi$, and $\overline{\alpha_\beta \langle B \rangle_\phi}$ is due to the BMR's emergence.

Figure 7 shows the poloidal flux generation rates for the subsurface layer at $r = 0.95R$. In our model, the mean-field α-effect makes the major contribution to the poloidal magnetic field generation. On average, the emerging BMRs contribute to the mean electromotive force with the same sign as the mean-field α-effect. The extended cycle in $\mathcal{E}^{\alpha}_{\phi}$ is due to the axisymmetric toroidal magnetic field (see Pipin & Kosovichev 2019). In addition, we see that the large-scale nonaxisymmetric magnetic field that results from the BMR evolution can produce a considerable contribution to the generation of the poloidal magnetic field. This effect is caused by the nonlinear coupling of the axisymmetric and nonaxisymmetric modes of the magnetic field and the non-linearity of the α-effect (Bigazzi & Ruzmaikin 2004).

Figure 8 shows that the large-scale evolution of the vector-potential of the poloidal field on the surface is largely determined by the dynamo wave propagation from the depth of the convection zone. The generation and diffusive parts of the turbulent part of the global dynamo are in close balance (cf, Figs. 8b–c).

To compare the results presented in Figure 6 with observations, we reconstruct the surface axisymmetric vector-potential from the radial magnetic field given by observations of Kit Peak and SDO/HMI. To estimate the time derivative of the reconstructed A, we smooth the data in time and filter out all variations with periods shorter than three years. The obtained time evolution of A shows a qualitative agreement with the dynamo model, see Fig.9(a). Similarly, the reconstructed $\partial_t A$ qualitatively agrees with the dynamo model.

To estimate the generation rate of the poloidal magnetic field from the surface data, we have to use an assumption about the integral balance of the generation rate and diffusive loss of the poloidal magnetic field in the turbulent dynamo (see Fig. 8). Results in Fig. 9a agree with the analysis of Knaack & Stenflo (2005). For this case, the generation rate of the poloidal flux is determined by the time derivative of the vector-potential at the equator. The previous analysis shows that this quantity is determined by diffusive propagation of the poloidal magnetic field dynamo wave from the depth of the convection zone. The qualitative agreement of results in Fig. 6 and Fig. 8 favors the same origin of the surface poloidal flux change in the solar dynamo. Interpretation of Fig. 8a–b in terms of the Babcock-Leighton scenario and the 1D dynamo models like that suggested by Cameron & Schüssler (2015, 2017) is difficult to accept. Indeed for the standard case, when the BMR, which satisfies the Hale and Joy laws, emerges at the surface, they do not immediately contribute to the large-scale poloidal flux generation. The contribution to the solar dynamo is related to their evolution by means of diffusion and meridional circulation. Although, the emergence of the "rogue" BMRs (Nagy et al. 2017) may produce an immediate effect on the large-scale poloidal variation. However, they do not represent a regular component of the solar dynamo.

Figure 10 shows the evolution of the axisymmetric poloidal magnetic field flux and its time derivative during Solar Cycles 21–24 as deduced from the magnetic measurements from Kit Peak Solar Observatory and SDO/HMI and the corresponding results of our dynamo model. Cycles 21 and 22 show the regular sinusoidal-like variations of the poloidal flux and its derivative. The maximum of the poloidal flux generation rate corresponds to the maximum of the magnetic cycle. The maxima of the magnetic cycles show strong variations in the generation rate because of the BMRs. Presumably, these variations are due to the "rogue" active regions near the solar equator. Interesting that the observations show that the poloidal flux generation rate fluctuated about zero for about five years at the end of Cycle 23. This corresponds to the plateau in the poloidal flux evolution. The dynamo model runs do not reproduce the plateau, instead showing a decrease in the production rate of the poloidal flux. Understanding this plateau requires further investigation. The plateau and the extended decay of Solar Cycle 23 are connected. There is no satisfactory explanation for this within the solar dynamo model. In the Babcock-Leighton scenario the extended decay of Cycle 23 and weak Cycle 24 were interpreted as a result of the emergence of "rogue" active regions during the growing phase of Cycle 23 Jiang et al. (2015). The suggestion of Dikpati et al. (2010) relates these phenomena to variations in the meridional circulation structure.

4. DISCUSSION AND CONCLUSIONS

Generation and decay of the axisymmetric toroidal and poloidal magnetic field fluxes govern the solar dynamo. Motivated by the results of Cameron & Schüssler (2015), we analyzed the components of the dynamo budget using solar observations and results of the mean-field dynamo models. One of the findings of CS15 was the crucial role of the surface differential rotation in the generation of the axisymmetric toroidal magnetic field of the Sun. Our results suggest that a subdominant role of the radial shear in the solar dynamo can result from the sign variation of the radial gradient of the angular velocity in the bulk of the convection zone. Nevertheless, it is important to maintain the average level of magnetic activity in the dynamo domain. Results of the 3D dynamo model show a higher generation rate of the toroidal flux by solar differential rotation than the axisymmetric 2D models.

We find that the toroidal flux generation rate by the surface differential rotation depends strongly on the radial magnetic field profile in the polar regions. Observations show that the radial magnetic field is almost uniform near solar poles during epochs of the solar minima, while the dynamo models show a sharp increase in the toroidal flux generation rate toward the poles. The toroidal flux generation rate by the latitudinal shear reaches the maximum at the poles both in the observations and dynamo models for the time of solar activity minima. This property explains the relative success of the correlation between the polar magnetic field strength and the magnitude of the subsequent magnetic cycle for the solar cycle predictions (Schatten et al. 1978; Choudhuri et al. 2007). Our results suggest that the correlation strength can depend on the profile of the radial magnetic field near solar poles. The long-term direct measurements of the large-scale solar magnetic fields in polar regions can help to resolve the issue.

The magnitude of the integral parameters for the surface poloidal magnetic field flux and its generation rate agree with the estimation of Cameron & Schüssler 2023. Our analysis suggests that a considerable part of the generated axisymmetric poloidal magnetic field flux comes from deep layers of the convection zone. The interpretation of the surface poloidal magnetic field evolution solely in terms of the Babcock-Leighton scenario, in which the axisymmetric poloidal flux is generated in situ of the BMR emergence, is difficult to accept. In the standard case, the emerging BMRs that follow the Hale and Joy laws do not immediately contribute to the large-scale poloidal flux generation. Their contribution is related to their subsequent evolution by means of diffusion and meridional circulation. The dynamo model shows that most part of the poloidal flux generation is due to the effect of the radial diffusion and propagation of the dynamo wave from the depth. Although the so-called "rogue" BMR (Nagy et al. 2017) can produce an immediate effect on the large-scale poloidal variation, they do not represent the regular component of the solar dynamo.

Acknowledgments

VP thanks the financial support of the Ministry of Science and Higher Education of the Russian Federation (Subsidy No.075-GZ/C3569/278). AK acknowledges the partial support of the NASA grants: NNX14AB70G, 80NSSC20K0602, 80NSSC20K1320, and 80NSSC22M0162.

Data Availability Statements. The data underlying this article are available by request.

REFERENCES

Abramenko, V. I., Suleymanova, R. A., & Zhukova, A. V. 2023, MNRAS, 518, 4746, doi: 10.1093/mnras/stac3338

Babcock, H. W. 1961, ApJ, 133, 572, doi: 10.1086/147060

Bigazzi, A., & Ruzmaikin, A. 2004, ApJ, 604, 944, doi: 10.1086/381932

Cameron, R., & Schüssler, M. 2015, Science, 347, 1333, doi: 10.1126/science.1261470

Cameron, R., & Schüssler, M. 2023, Observationally guided models for the solar dynamo and the role of the surface field. https://arxiv.org/abs/2305.02253

Cameron, R. H., & Schüssler, M. 2017, A&A, 599, A52, doi: 10.1051/0004-6361/201629746

Choudhuri, A. R., Chatterjee, P., & Jiang, J. 2007, Physical Review Letters, 98, 131103, doi: 10.1103/PhysRevLett.98.131103

Choudhuri, A. R., & Dikpati, M. 1999, SoPh, 184, 61

Dikpati, M., Gilman, P. A., de Toma, G., & Ulrich, R. K. 2010, Geophys. Res. Lett., 37, L14107, doi: 10.1029/2010GL044143

Getling, A. V., Kosovichev, A. G., & Zhao, J. 2021, ApJL, 908, L50, doi: 10.3847/2041-8213/abe45a

Jiang, J., Cameron, R. H., & Schüssler, M. 2015, ApJL, 808, L28, doi: 10.1088/2041-8205/808/1/L28

Karak, B. B., Jiang, J., Miesch, M. S., Charbonneau, P., & Choudhuri, A. R. 2014, SSRv, 186, 561, doi: 10.1007/s11214-014-0099-6

Kitchatinov, L. L., & Pipin, V. V. 1993, A&A, 274, 647

Kitchatinov, L. L., & Rüdiger, G. 1992, A&A, 260, 494

Knaack, R., & Stenflo, J. O. 2005, A&A, 438, 349, doi: 10.1051/0004-6361:20052765

Komm, R. 2022, SoPh, 297, 99, doi: 10.1007/s11207-022-02027-z

Komm, R., González Hernández, I., Howe, R., & Hill, F. 2015, SoPh, 290, 3113, doi: 10.1007/s11207-015-0729-5

Komm, R., Howe, R., & Hill, F. 2018, SoPh, 293, 145, doi: 10.1007/s11207-018-1365-7

Kosovichev, A. G., & Pipin, V. V. 2019, ApJ, 871, L20, doi: 10.3847/2041-8213/aafe82

Krause, F., & Rädler, K.-H. 1980, Mean-Field Magnetohydrodynamics and Dynamo Theory (Berlin: Akademie-Verlag), 271

Kumar, R., Jouve, L., & Nandy, D. 2019, A&A, 623, A54, doi: 10.1051/0004-6361/201834705

Leighton, R. B. 1969, ApJ, 156, 1, doi: 10.1086/149943

Mitra, D., Candelaresi, S., Chatterjee, P., Tavakol, R., & Brandenburg, A. 2010, Astronomische Nachrichten, 331, 130, doi: 10.1002/asna.200911308

Nagovitsyn, Y. A., Tlatov, A. G., & Nagovitsyna, E. Y. 2016, Astronomy Reports, 60, 831, doi: 10.1134/S1063772916090055

Nagy, M., Lemerle, A., Labonville, F., Petrovay, K., & Charbonneau, P. 2017, SoPh, 292, 167, doi: 10.1007/s11207-017-1194-0

Parker, E. 1955, Astrophys. J., 122, 293

Parker, E. N. 1984, ApJ, 281, 839, doi: 10.1086/162163

Paxton, B., Cantiello, M., Arras, P., et al. 2013, ApJS, 208, 4, doi: 10.1088/0067-0049/208/1/4

Pipin, V. V. 2018, Journal of Atmospheric and Solar-Terrestrial Physics, 179, 185, doi: 10.1016/j.jastp.2018.07.010

—. 2022, MNRAS, 514, 1522, doi: 10.1093/mnras/stac1434

Pipin, V. V., & Kosovichev, A. G. 2019, ApJ, 887, 215, doi: 10.3847/1538-4357/ab5952

—. 2020, ApJ, 900, 26, doi: 10.3847/1538-4357/aba4ad

Pipin, V. V., Kosovichev, A. G., & Tomin, V. E. 2022, arXiv e-prints, arXiv:2210.08764, doi: 10.48550/arXiv.2210.08764

Rempel, M. 2005, ApJ, 631, 1286, doi: 10.1086/432610

Ruediger, G., & Brandenburg, A. 1995, A&A, 296, 557

Schatten, K. H., Scherrer, P. H., Svalgaard, L., & Wilcox, J. M. 1978, Geophys. Res. Lett., 5, 411, doi: 10.1029/GL005i005p00411

Schrijver, C., & Harvey, K. 1984, Sol.Phys., 150, 1

Schrijver, C. J., & Harvey, K. L. 1994, SoPh, 150, 1, doi: 10.1007/BF00712873

Wilson, P. R., Altrocki, R. C., Harvey, K. L., Martin, S. F., & Snodgrass, H. B. 1988, Nature, 333, 748, doi: 10.1038/333748a0

Yoshimura, H. 1975, ApJ, 201, 740, doi: 10.1086/153940

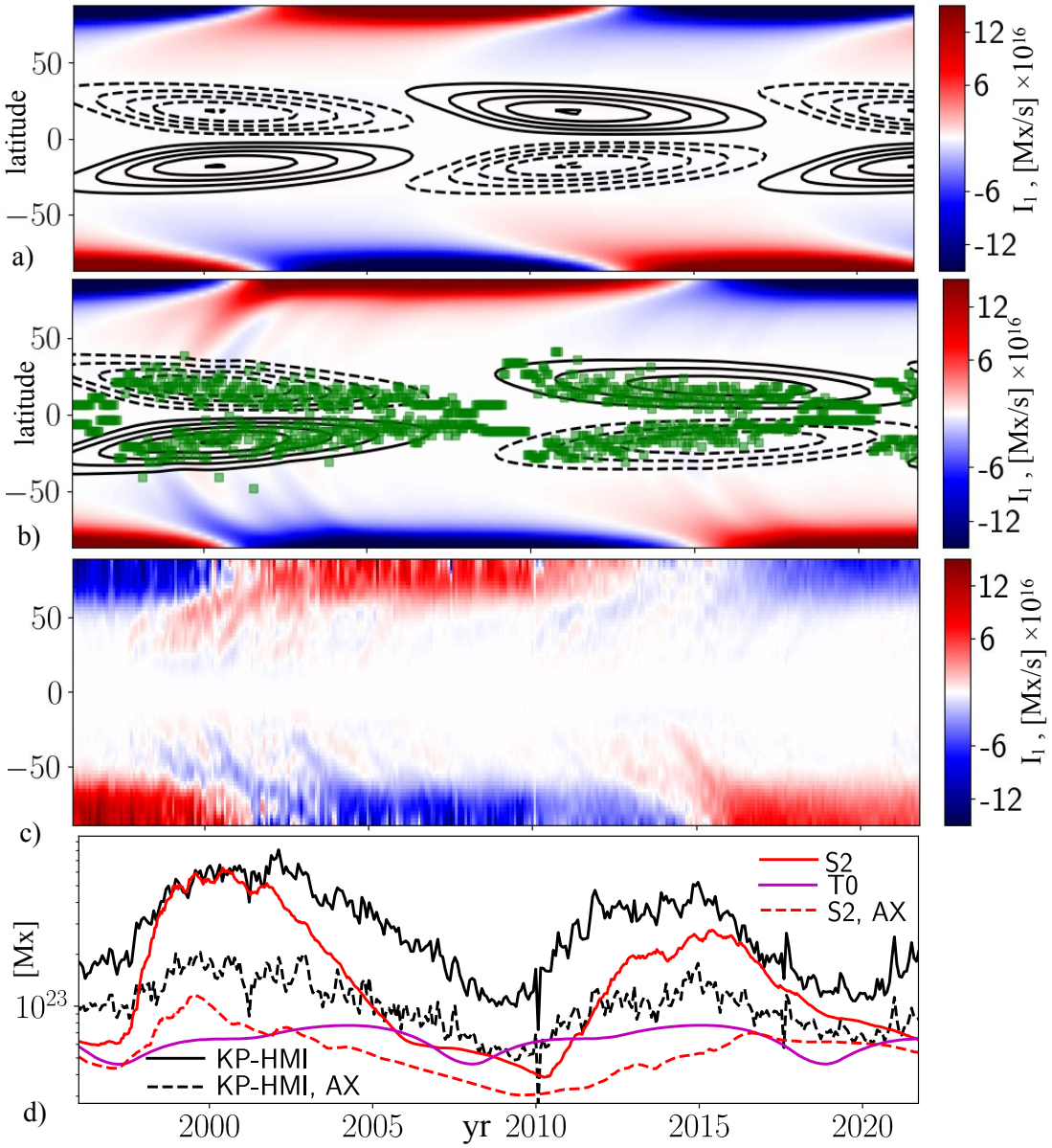

Figure 1. Panels a) and b) show the time-latitude diagram of the near-surface toroidal magnetic field (contours in the range of ±1kG) for Models T0 and S2; the background color shows the flux generation rate of the toroidal magnetic field from the surface differential rotation, i.e., integral kernel I_1 of Eq. (2); the green squares in panel (b) mark positions of the initiated BMR; c) the same as in panel (b) for the axisymmetric magnetic field from the Kitt Peak Observatory (KPO) and SDO/HMI synoptic maps; d) shows the total unsigned flux of the radial magnetic field at the surface for the dynamo models and observations, where KP-HMI, AX marks results for the axisymmetric magnetic field obtained from the combined data of KPO and SDO/HMI, and the "S2,AX" curve shows the axisymmetric magnetic flux variations calculated from the nonaxisymmetric dynamo model.

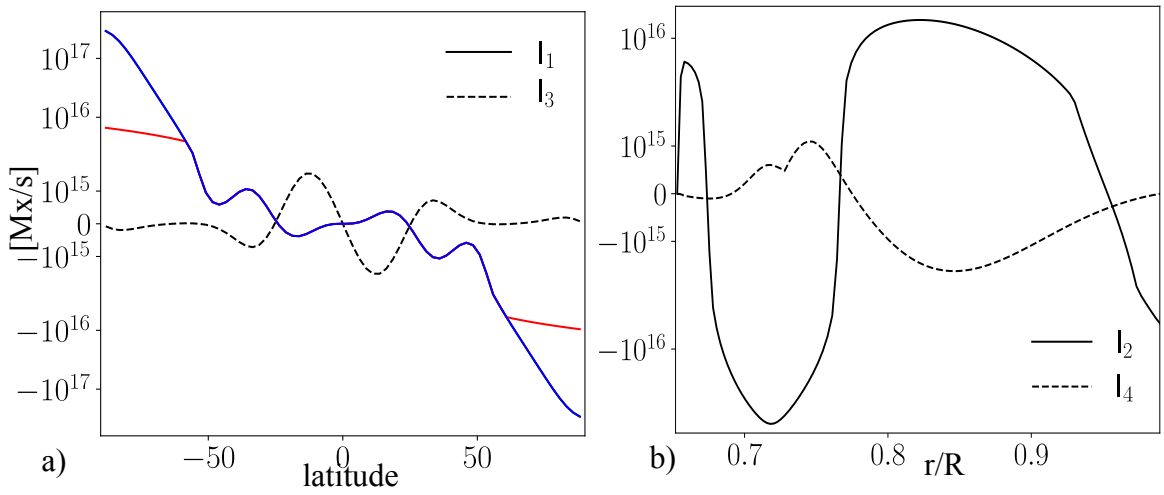

Figure 2. Estimation of contributions to the flux budget Eq. (2) for the cycle minima. The red lines in panel a) show I_1 for the assumption of constant $\overline{B}_r$ in high-latitude regions above 60° latitude.

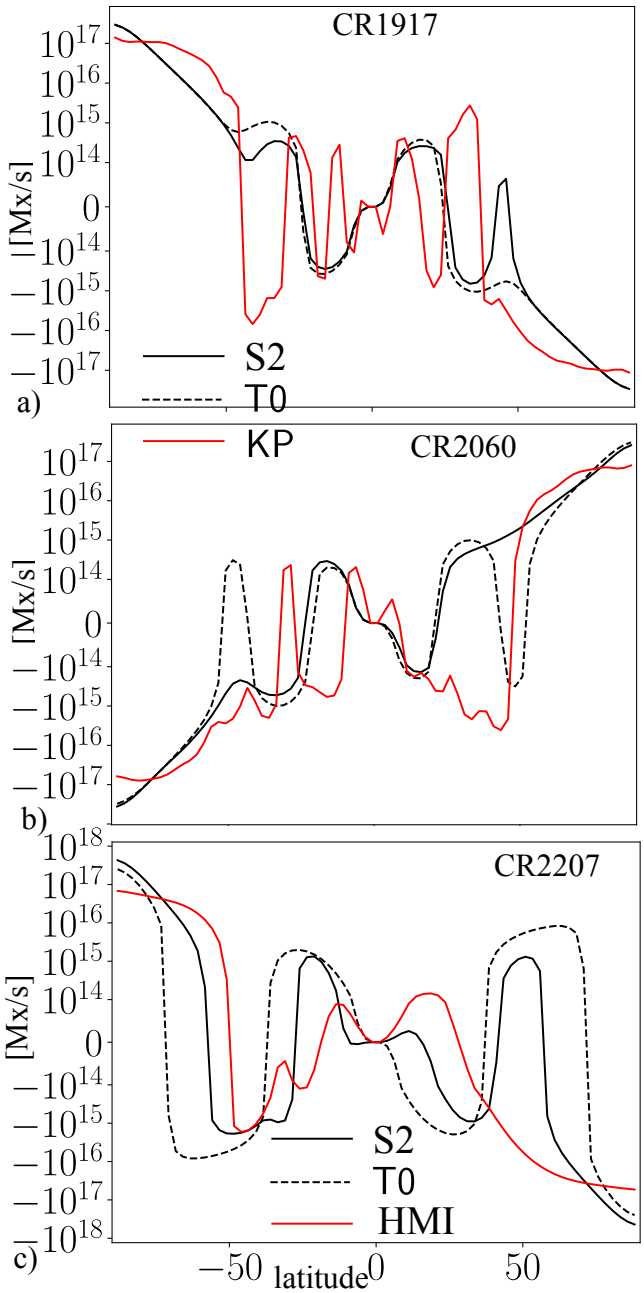

Figure 3. Estimation of contributions of the toroidal magnetic field generation rate from the surface magnetic field, see Eq. (2), for the minima of Cycles 22, 23, and 24 in our dynamo models and the observations.

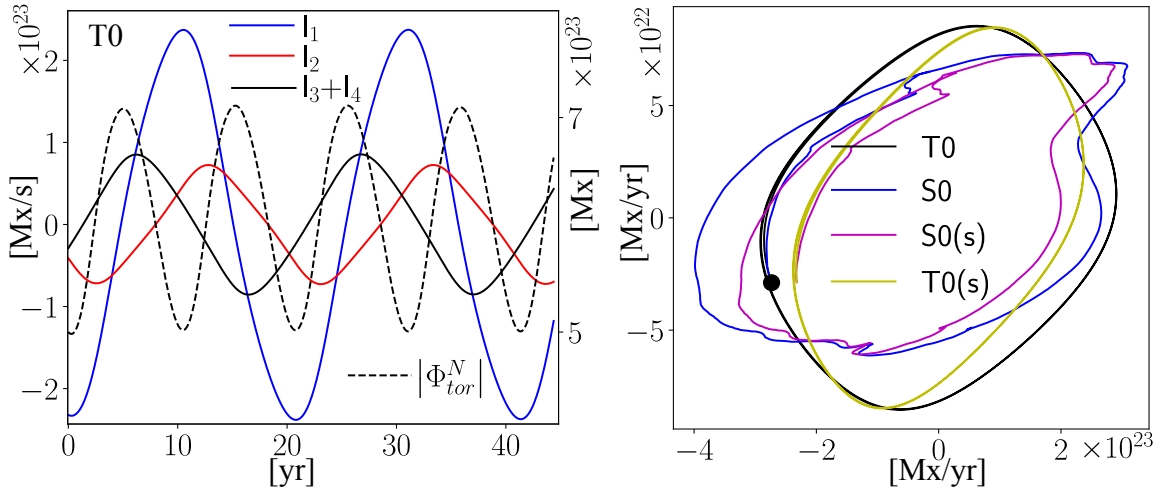

Figure 4. a) Time evolution of the RHS contributions of Eq.2 for Model T0; b) the phase diagram of the toroidal flux generation (horizontal axis) and loss (vertical axis) rates; the black curve shows Model T0, green line - the same run (T0a) where the radial subsurface shear (region r=0.9-0.99R) is neglected, the yellow curve shows the budget for Model T0, where we assume that $\overline{B}_r$ is constant above 60° latitude (S0(s),T0(s)), the blue and red curves show Models S0 and T0 and the magenta line shows Model S0, the budget of which includes only the surface contributions ($I_{1,3}$). Circles mark the model starting points.

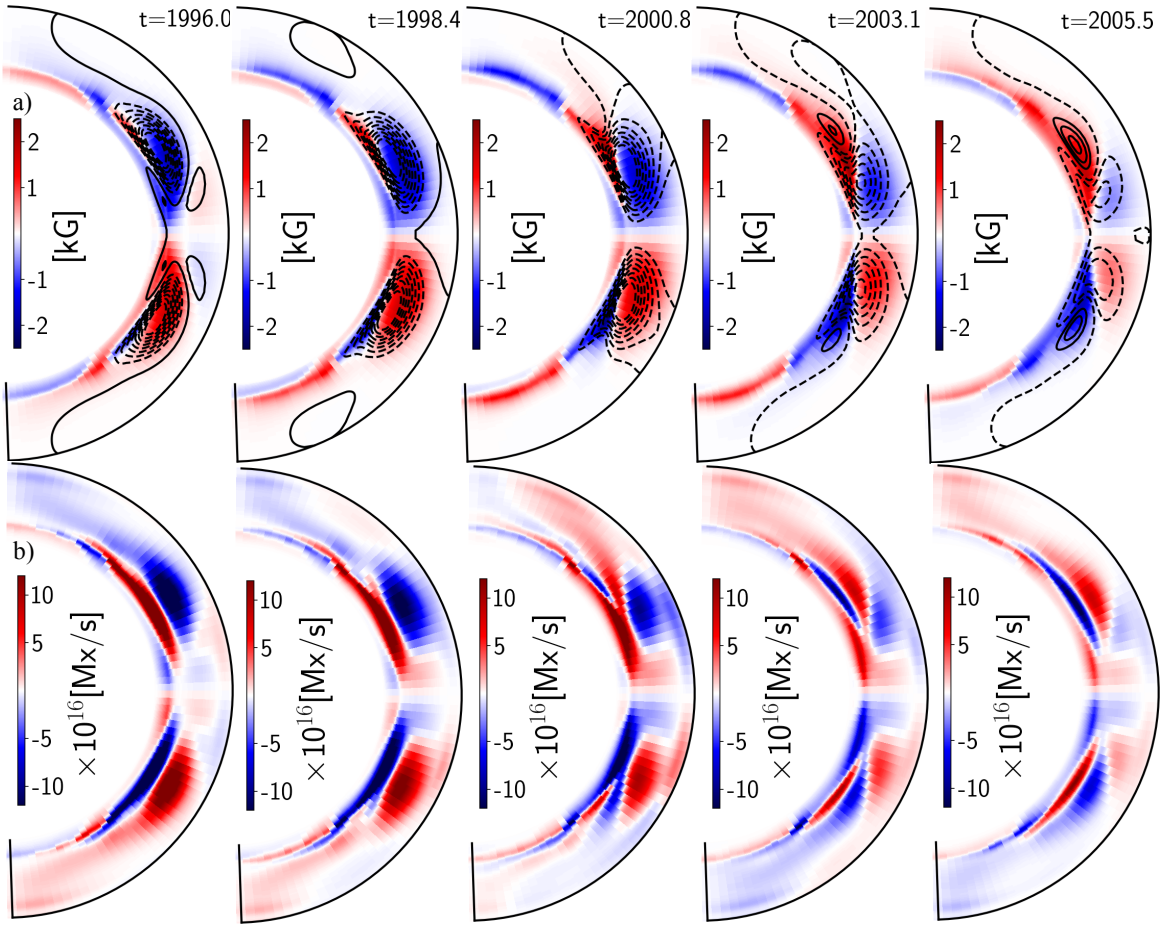

Figure 5. a) The evolution of the axisymmetric toroidal magnetic field (images) and the vector-potential of the poloidal field during Cycle 23 in Model S2, illustrating the dynamo wave propagation in the convection zone; b) the corresponding toroidal flux generation rate (see animation of this Figure in the online version).

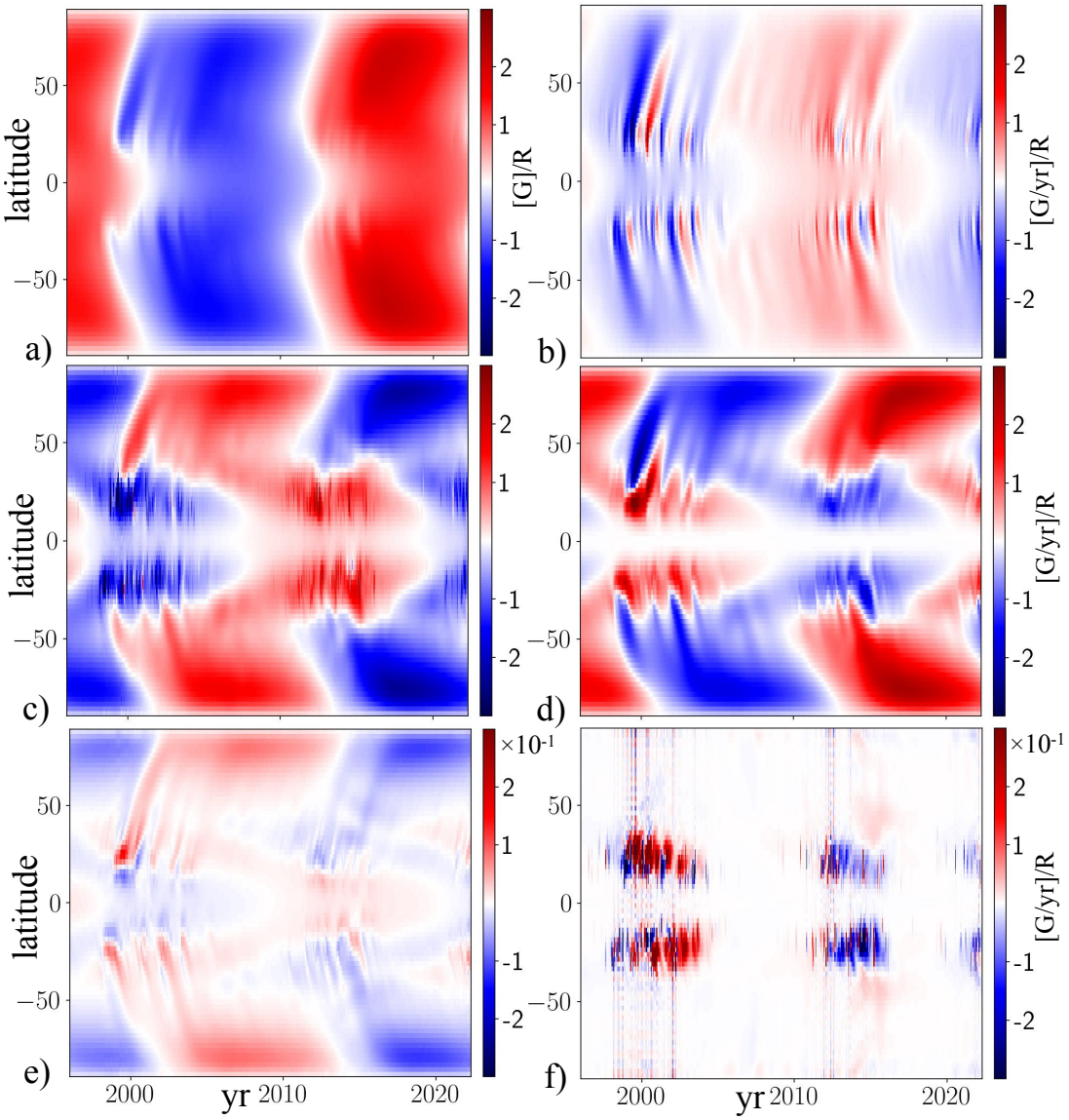

Figure 6. Panels a) and b) show the time-latitude diagrams of vector-potential A and its derivative $\partial_t A$. Other panels show the same for the different terms in the vector-potential evolution (see Eq.(4)); c) shows the effect of the radial diffusion; d) shows the effect of the meridional circulation; e) and f) show the effect of the latitudinal diffusion and the α-effect generation term $\mathcal{E}^{\alpha}_{\phi}$, respectively (noteworthy, they are of an order of magnitude smaller than other terms of the vector-potential evolution equation).

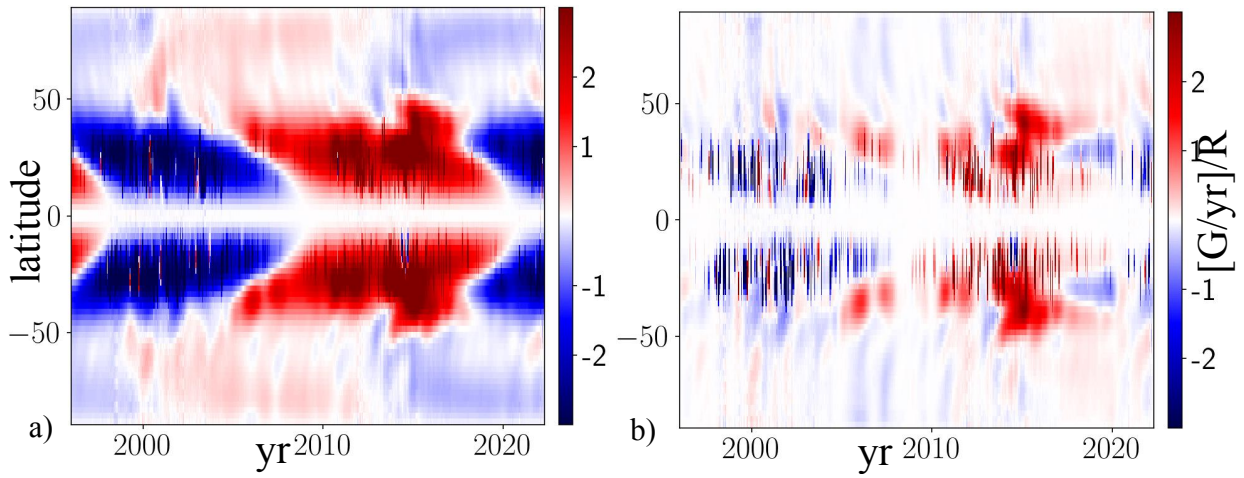

Figure 7. Time-latitude diagrams of the poloidal magnetic field generation rates at $r = 0.95R$, a) shows the total $\mathcal{E}^{\alpha}_{\phi}$, b) shows the effects due to the BMR activity and the nonaxisymmetric magnetic field, $\overline{\tilde{\alpha}_{\phi\phi}\tilde{B}_{\phi}} + \overline{\alpha_{\beta}\langle B\rangle_{\phi}}$ (note that the time scales of $\overline{\tilde{\alpha}_{\phi\phi}\tilde{B}_{\phi}}$ are longer than those for $\overline{\alpha_{\beta}\langle B\rangle_{\phi}}$) ;

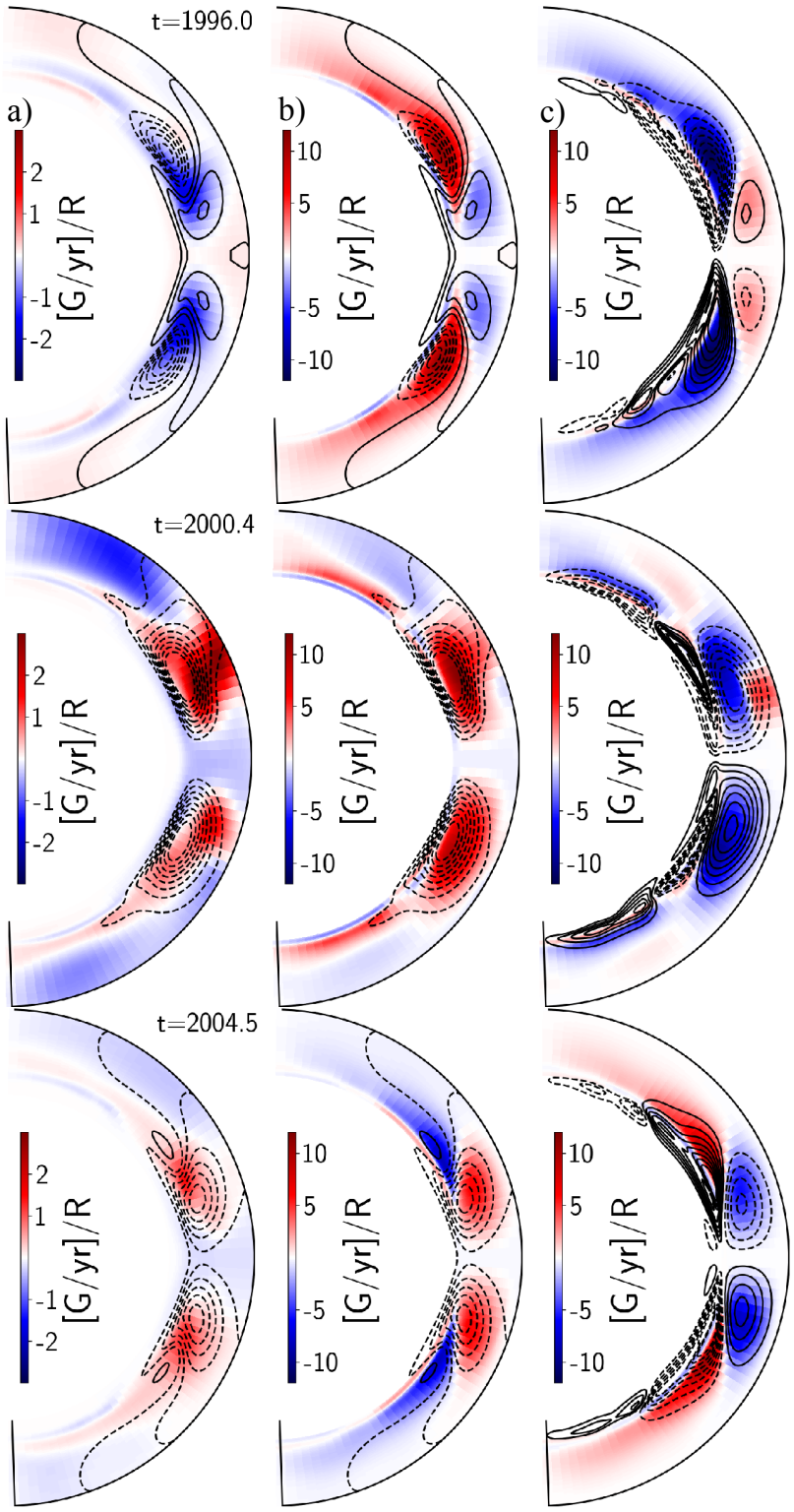

Figure 8. a) Snapshots of the vector-potential (streamlines of the poloidal magnetic field) and its time-derivative (color image) for the different phases of the modeled Cycle 23 in the meridional cross-section of the convection zone; b) the same as a) and color image shows contributions of the latitudinal meridional circulation, and all turbulent effects, except the generation term, $\mathcal{E}_\phi^\alpha$; c) shows the toroidal magnetic field contours in the range of $\pm$2kG and the color images show the generation effect, $\mathcal{E}_\phi^\alpha$

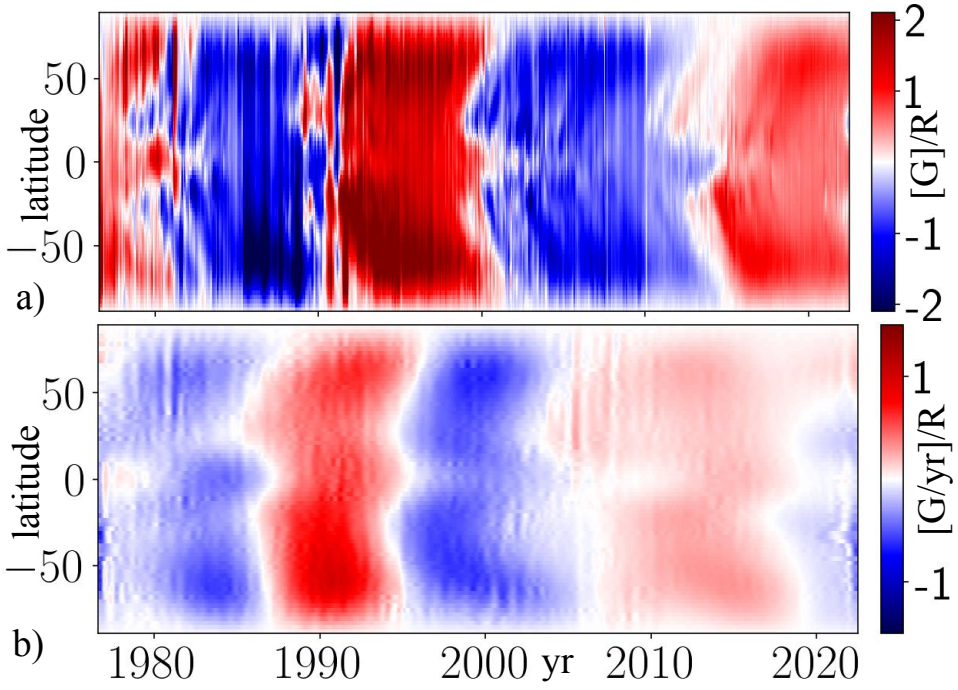

Figure 9. The same as in Figure 6 a) and b) for the KPO and SDO/HMI data set. Panel a) shows the evolution of the axisymmetric vector-potential; b) shows the estimation of $\partial_t A$ (for this quantity, we smooth A and filter out all harmonics with periods shorter than three years).

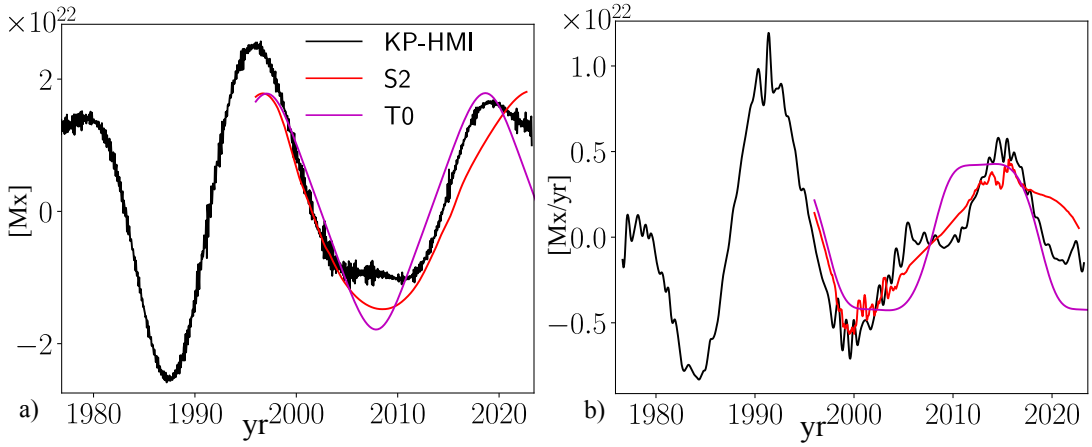

Figure 10. a) The black lines show the poloidal flux in the Northern hemisphere (left y-axis) as deduced from the observations (solid black line) and the dynamo models (color lines); b) the corresponding time derivatives of the poloidal flux.